OPEN ACCESS

Impact of CeCo-Coated Metallic Interconnectors on SOCs Towards Performance, Cr-Oxide-Scale, and Cr-Evaporation

To cite this article: C. Grosselindemann *et al* 2024 *J. Electrochem. Soc.* **171** 054508

Journal of The Electrochemical Society, 2024 **171** 054508

Impact of CeCo-Coated Metallic Interconnectors on SOCs Towards Performance, Cr-Oxide-Scale, and Cr-Evaporation

C. Grosselindemann,[1,z] M. J. Reddy,[2] H. Störmer,[3] D. Esau,[1] M. Dorn,[1] F. M. Bauer,[4] D. Ewald,[1] L. Wissmeier,[5] J. Froitzheim,[2,*] and A. Weber[1,*]

[1]*Institute for Applied Materials—Electrochemical Technologies (IAM-ET), Karlsruhe Institute of Technology (KIT), Karlsruhe, D-76131, Germany*
[2]*Chalmers University of Technology, Department of Chemistry and Chemical Engineering, Gothenburg, Sweden*
[3]*Laboratory for Electron Microscopy (LEM), Karlsruhe Institute of Technology (KIT), Germany*
[4]*European Institute for Energy Research (EIFER), D-76131 Karlsruhe, Germany*
[5]*Kerafol Keramische Folien GmbH & Co. KG, Eschenbach, D-92676, Germany*

The performance of a solid oxide cell (SOC) depends on the operating environment. Regarding single cell tests with ideal contacting (gold, platinum, nickel meshes) and inert flow fields (Al_2O_3), performance is limited by intrinsic losses in the cell. Contact losses and poisoning effects are minimized. In a SOC-stack with metallic interconnectors, performance is affected by contact resistances, chromium (Cr) evaporation, and limitations in gas supply. Here, 1 cm^2 single cells were tested with a stack-like contact applying metallic flow fields made from three different steel grades (Crofer 22 APU, AISI 441, UNS S44330) with and without a cerium-cobalt PVD-coating. Cell performance and losses were analyzed by IV-characteristics, impedance spectroscopy, and DRT analysis. For all uncoated interconnectors, significant performance losses due to increased contact losses and air electrode polarization were observed, which is attributed to Cr-oxide scale formation on the metallic interconnectors and Cr-poisoning of the air electrode as revealed by scanning electron microscopy-energy-dispersive X-ray spectroscopy. A CeCo-coating leads to similar oxide scales irrespective of the substrate material. Moreover, with the coating the electrochemical performance drastically improved due to decreased contact losses and an effective blocking of Cr-evaporation leading to a cell performance close to the ideal case for all three steel grades.

 [DOI: 10.1149/1945-7111/ad44da]

Manuscript submitted February 2, 2024; revised manuscript received April 23, 2024. Published May 10, 2024. *This paper is part of the JES Focus Issue on SOFC XVIII: Advances in Solid Oxide Fuel Cell and Electrolysis Cell Technology.*

Nomenclature

Latin letters

c	Counts (-)
E	Energy (keV)
j	Current density (A m^{-2})
R_0	Ohmic resistance (Ω m^2)
R_{pol}	Polarization resistance (Ω m^2)
$R_{contact}$	Contact resistance (Ω m^2)
T	Temperature (K)
U_{cell}	Cell voltage (V)
$\bar{x}_{Cr}$	Mean value of chromium content (at%)

Greek letters

δ	Concentration of oxygen lattice vacancy (−)
η	Overpotential (V)
φ	Potential (V)
σ	Standard deviation

Subscripts

AE	Air electrode
cell	Cell
EL	Electrode
FE	Fuel electrode
H_2	Hydrogen
H_2O	Steam
mesh	Contact mesh
MIC	Metallic Interconnector
pol	Polarization
probe	Probe

Abbreviations

AE	Air electrode
Al_2O_3	Aluminum oxide
APS	Atmospheric plasma spraying
ASR	Area specific resistance
Au	Gold
Ce	Cerium
Co	Cobalt
Cr	Chromium
EDXS	Energy-Dispersive X-ray Spectroscopy
Fe	Iron
GDC	Gadolinium-Doped Ceria
IV	Current-voltage
MIC	Metallic Interconnector
Mn	Manganese
DRT	Distribution of relaxation times
EIS	Electrochemical impedance spectroscopy
EL	Electrode
ESC	Electrolyte-supported cell
FE	Fuel electrode
H_2	Hydrogen
H_2O	Steam
La	Lanthanum
LSCF	$La_wSr_xCo_yFe_zO_{3-\delta}$
Ni	Nickel
O_2	Oxygen molecule
O	oxygen
OCV	Open-circuit-voltage
PVD	Physical-vapor deposition
SEM	Scanning Electron Microscopy
Sr	Strontium
SOC	Solid oxide cell
3YSZ	3 mol% yttria-stabilized zirconia

Metallic interconnectors (MICs)[1,2] are crucial for the contacting of planar high-temperature solid oxide cells[3] (SOC) in a stack in order to reach out for large scale industrialization for the production of electricity (SOFC), hydrogen (H_2) and/or mixtures of hydrogen and carbon monoxide (synthesis gas).[4–6] MICs have an economic

*Electrochemical Society Member.
[z]E-mail: cedric.grosselindemann@kit.edu

benefit regarding material and manufacturing costs as well as easier machinability in comparison to ceramic flow fields.[1,2,7–9] These can be made of chromia based alloys or ferritic stainless steels with the ability to form a chromium (Cr) oxide layer.[10–13] Ferritic stainless steels take advantage in machinability, costs, mechanical properties and have a moderately conductive oxide scale.[11,14,15] The steel grade Crofer 22 APU, tailormade for MIC, is extensively studied and used in commercialized stacks for fuel cell as well as electrolysis mode.[15–17] Numerous further steel grades such as AISI 441, 444, 430, 409 and others were investigated in literature.[18–23] In order to minimize Cr-evaporation and corrosion from the MIC, protective coatings need to be applied especially on the air side.[14,24,25] This decreases chromium poisoning of the air electrode and the contact resistance between electrode and MIC. Different techniques are available in order to apply various types of coatings.[1,26–28] They can be applied by physical vapor deposition (PVD),[24] wet powder spraying (WPS),[29] atmospheric plasma spraying (APS),[27,30,31] screen printing,[32–35] electrophoretic deposition[36] and sol-gel processing.[37] A self-healing effect was observed for a manganese-cobalt-iron oxide coating applied by APS.[30,38] Long-term stability for 40 kh of operation was shown in Refs. 39–41 for Crofer 22 APU fully coated with a (Co, Mn, Fe)$_3$O$_4$ spinel oxide. Different contact layers at the air side were investigated by Kusnezoff et al.[42]

In this work, 3 different steel grades (Crofer 22 APU, AISI 441, UNS S44330) are investigated in the uncoated and coated state. A protective coating of cerium-cobalt (CeCo) is applied by a PVD-process. The CeCo protective layer is a commercialized product (Sanergy^{TM} HT) by Alleima AB[43] (former Sandvik Materials Technology), which can be applied in a high volume large scale roll to roll coating process on any ferritic stainless steel grade. The protective layer consists of a top layer of metallic Co with approx. 600 nm and a Ce layer in the range of 10–20 nm.[24] This type of coating was proven to be suitable for stable long-term operation of nearly 40 kh[44] and holds self-healing properties as well.[45] In the work by Norrby et al.[46] a CeCo coated steel grade (AISI 441) was exposed at 800 °C in air in a box furnace for 87700 h and showed no sign of breakaway corrosion.

In a previous study by Reddy et al.[18] different steel grades (AISI 441, 444, 430, 409) were investigated in the uncoated and coated (CeCo) state by time-resolved mass gains, chromium evaporation (denuder technique[47]) and measurements of the area-specific resistance (ASR). A different oxidation rate as well as Cr-evaporation was found between the uncoated steels. By applying a commercialized PVD coated CeCo layer the Cr-evaporation rate was reduced by 60–100%.[18] For the uncoated steels in Ref. 18 a chromium manganese ((Cr,Mn)$_3$O$_4$) layer is formed at the surface of the MIC. In comparison, a cobalt manganese ((Co,Mn)$_3$O$_4$) layer at the surface results from the coated samples.[18]

To analyze the performance on the single cell level[48,49] effects resulting from the MIC like chromium poisoning,[20,50–53] corrosion[9,54] as well as increased contact and gas diffusion losses need to be omitted. This requires the application of an inert testing environment with ceramic flow fields and noble metal contact grids in order to analyze the ideal cell performance.[55–57] The electrochemical characterization under ideal conditions has been shown for various anode-supported cells[48,56–58] as well as for electrolyte-supported cells (ESC).[5,59,60]

To investigate the different impacts of a stack like contacting on the cell performance, individual effects can be mimicked in a single cell test. This can for example be realized by an upstream chromium source[50] or a metallic flow field in combination with a noble metal contact mesh[20] that avoids further impacts related to increased contact and gas diffusion resistances or a stack like flow field made from noble metal that just mimics limited gas diffusion and inhomogeneous contacting of the electrode.[61]

This work focusses on the investigation of loss contributions related to the interconnector material, coatings and cell contacting/gas supply. Single cells were tested with a stack-like contacting

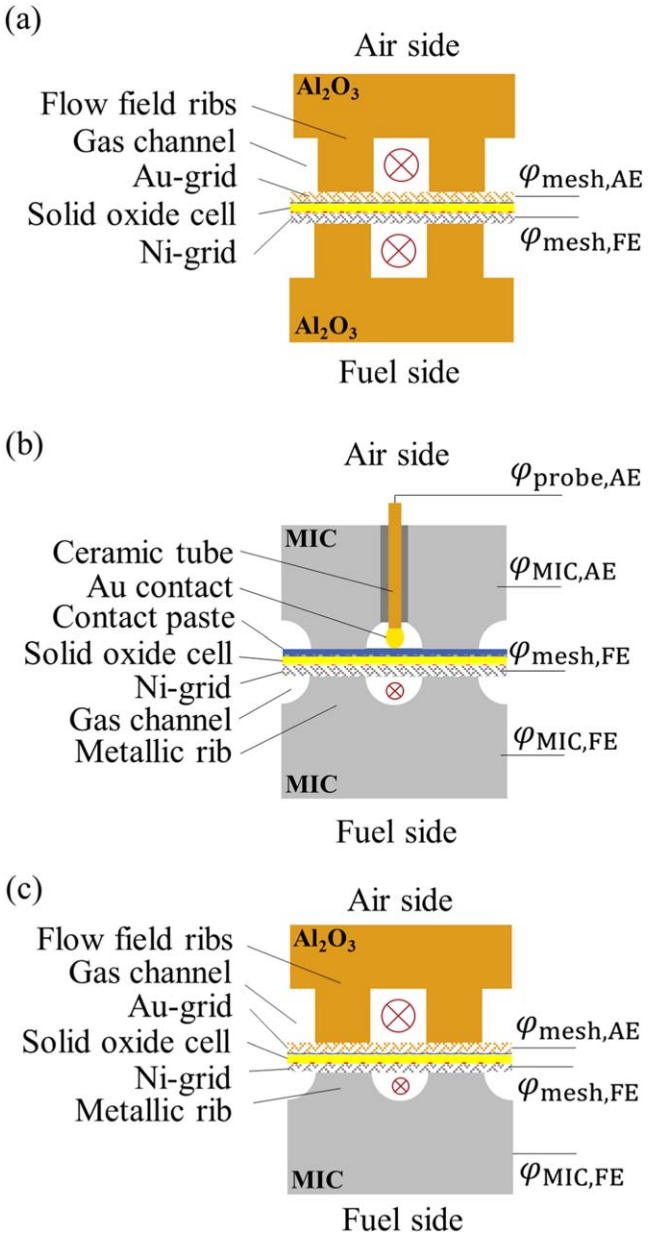

Figure 1. (a) Ideal contacting with ceramic flow fields and contact grids of Ni (fuel side) and gold (Au) (air side) and (b) stack-like contacting with metallic interconnectors with welded Ni-grid (fuel side) and screen printed LSCF contact paste layer (air side) with potential probes. (c) MIC with welded Ni-grid at the fuel side and a ceramic flow field with gold mesh at the air side.

applying a single metallic flow field geometry made from three different steel grades (Crofer 22 APU (1.4760), AISI 441 (1.4509), UNS S44330 (1.4622)) with and without a cerium-cobalt PVD-coating.[18,28,62] Cell performance and losses are evaluated by IV-characteristics, impedance spectroscopy and DRT-analysis. Based on a method developed by Kornely et al.[61] the contact loss between the MIC and the electrode is evaluated. The results of the electrochemical characterization are correlated to the Cr-oxide scale formed on the interconnectors and the existence of Cr-compounds in the air electrode. Microstructural analysis[18] of the different tested metallic interconnectors is performed by scanning-electron-microscopy (SEM) and energy-dispersive X-ray spectroscopy (EDXS). The air electrodes are investigated by SEM-EDXS when in contact with all un-/coated MICs of this work.

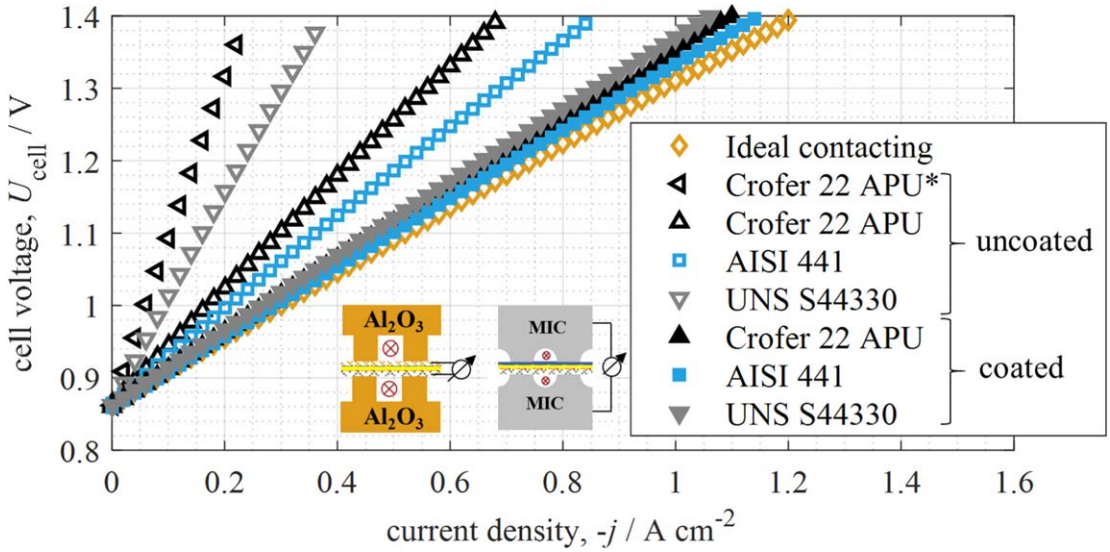

Figure 2. IV-Characteristics of ideal contacting, Crofer 22 APU* (uncoated and without contact paste), un-/coated Crofer 22 APU, AISI 441 and UNS S44330 in electrolysis mode at T = 850 °C with 0.20 atm H_2 (balance H_2O) and air at the air electrode.

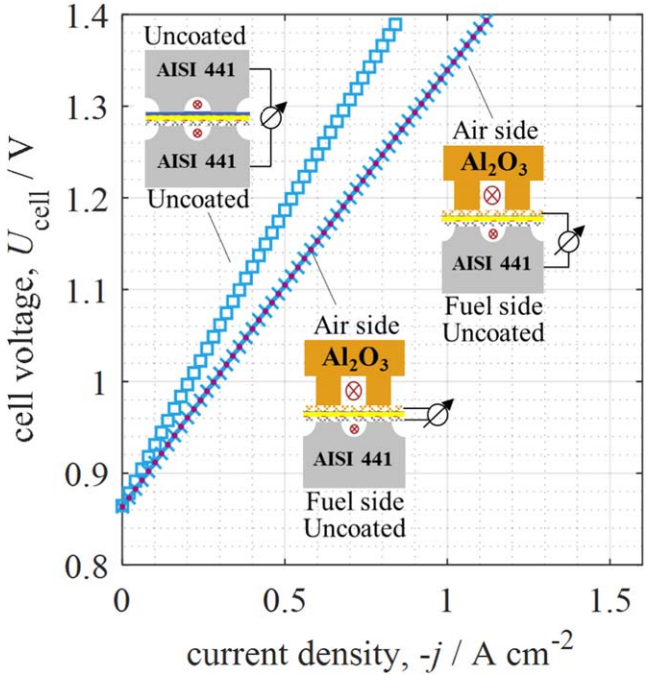

Figure 3. IV-Characteristics of AISI 441 (MIC both sides uncoated and MIC uncoated fuel side only) in electrolysis mode at T = 850 °C with 0.20 atm H_2 (balance H_2O) and air at the air electrode.

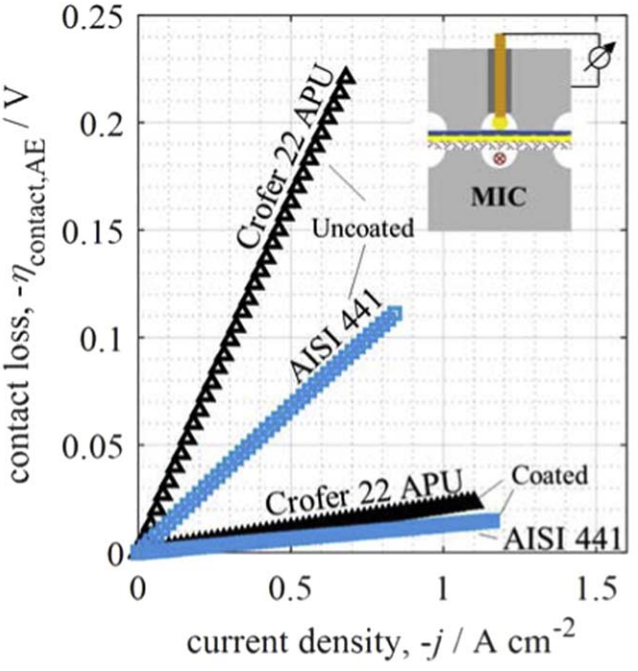

Figure 4. Contact loss of un-/coated Crofer 22 APU and AISI 441 in electrolysis mode at T = 850 °C with 0.20 atm H_2 (balance H_2O) and air at the air electrode.

Experimental

Planar electrolyte-supported cells with an active cell area of 1 cm^2 were investigated in this study. The cells exhibited a Ni/GDC fuel electrode, 3YSZ electrolyte substrate[63] and an LSCF air electrode. Additional GDC layers were placed in between electrodes and electrolyte. Details on the cell microstructure including scanning electron microscope (SEM) images can be found in Refs. 60, 63.

Electrochemical characterization.—Measurements were performed with full cells in a test rig described in Ref. 64 At each electrode side a total flow rate of 250 sccm was set. Steam is produced in an upstream combustion chamber by mixing oxygen to the fuel. This enables a stable fuel humidification of up to 100% steam.

Ideal contacting is realized by an inert testing environment with respect to a ceramic (Al_2O_3) cell housing and flow fields as shown in Fig. 1a.[64] Contacting of the electrode is realized by finely meshed double-layered grids with Ni at the fuel and gold at the air electrode. Contact losses resulting from this setup can be neglected.[56,60,64] The cell voltage U_{cell} results from the difference between the potential measurements between the Ni grid ($\varphi_{mesh,FE}$) and gold grid ($\varphi_{mesh,AE}$). Gas transport conditions are shown schematically in Fig. 1a and in detail in Ref. 60.

With respect to a stack-like contacting as shown in Fig. 1b metallic flow fields exhibiting a model geometry were manufactured from different steel grades Crofer 22 APU, AISI 441 and UNS S44330 by milling. To enable a uniform coating by physical vapor deposition (PVD) a flow field geometry with round channels (0.5

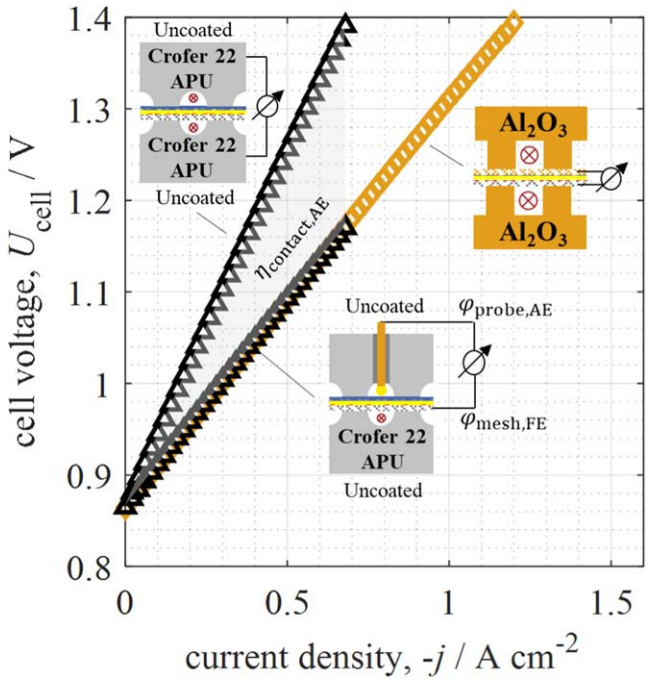

Figure 5. IV-Characteristics of ideal contacting and uncoated Crofer 22 APU with measured potential difference between $\varphi_{MIC,FE}$ and $\varphi_{MIC,AE}$ as well as $\varphi_{mesh,FE}$ and $\varphi_{probe,AE}$ in electrolysis mode at $T = 850$ °C with 0.20 atm H_2 (balance H_2O) and air at the air electrode and corresponding contact loss $\eta_{contact,AE}$ indicated in grey area.

mm radius) was chosen. The chemical composition of the specific batches of the three steel grade substrates is listed in the appendix in Tables A·1 and A·2. In comparison Crofer 22 APU has the highest content of chromium and AISI 441 having the least. To minimize Cr evaporation from uncoated parts of the samples,[65] CeCo (10 nm/600 nm) was deposited on all sides and edges of the sample. The depositions were done by Alleima AB using a batch PVD coater which realizes thin films in the nanometer range by evaporation of metallic Ce and Co in vacuum.

To establish a stack like contacting between electrode and metallic flow field, additional contact layers are applied. A single-layered Ni-grid is point welded onto the MIC at the fuel side. Regarding the air side, an LSCF contact paste is screen printed onto the air electrode and mounted in the liquid state.

The resulting contact losses mainly related to the contact between electrode and contact layer, i.e. oxide scales on the steel, can be quantified with a measurement technique by Kornely et al.[61] Potential probes are connected to the nickel mesh as well as to the MIC at the fuel side as shown in Fig. 1b. The difference of the measured potential probes of the metallic interconnector $\varphi_{MIC,FE}$ and the contact mesh $\varphi_{mesh,FE}$ results in the contact voltage loss $\eta_{contact,FE}$ at the fuel electrode (FE) in Eq. 1.

$$\eta_{contact,FE} = \varphi_{MIC,FE} - \varphi_{mesh,FE} \quad [1]$$

At the air side the potential is likewise measured at the MIC. To access the potential of the LSCF contact layer, a ceramic capillary with a gold wire ending on top of the contact layer surface is plugged through a drilled hole in the MIC (Fig. 1b). Thus, the potential at this point can be measured and likewise the corresponding voltage loss $\eta_{contact,AE}$ is defined in Eq. 2 by the difference between the metallic interconnector $\varphi_{MIC,AE}$ and the probe $\varphi_{probe,AE}$ at the air electrode (AE).

$$\eta_{contact,AE} = \varphi_{MIC,AE} - \varphi_{probe,AE} \quad [2]$$

It should be noted that $\eta_{contact,AE}$ includes the contact losses and the losses resulting from the in-plane conduction in the air electrode.[61] In case of an LSCF electrode and additional LSCF contact layer the latter can be neglected.[66]

Further, Fig. 1c shows a variation of the contact set-up with a metallic flow field at the fuel side and a ceramic flow field at the air side in order to allocate the impact of enhanced gas diffusion at the MIC-contacted fuel electrode.

A predefined startup procedure was performed once the cell is placed in the test rig. Sufficient drying and sintering of the initially liquid LSCF contact layer was realized at 850 °C in air for 24 h. In the following testing phase, impedance spectra and IV-characteristics were measured at systematically varied operating conditions. The spectra were acquired by a Zahner Zennium E frequency response analyzer.[64] The frequency was varied in between 30 mHz and 10^5 Hz with 12 points per decade. All spectra were measured under open circuit conditions (OCV). The validity of the spectra was verified by a Kramers Kronig Test.[67]

Degradation effects during the rather short test of approx. 200 h were evaluated from reference measurements at start and end of test. Whereas the ideal contacted cell as well as all experiments with coated MICs showed nearly no performance change (< 5%), in case of uncoated MICs a significant degradation (10%–40%) was observed. For reasons of comparison spectra and IV-characteristics of tests with uncoated MICs were taken at the start of test.

EDXS metallic interconnectors.—The tested un-/coated metallic interconnectors were analyzed post-mortem by preparing cross-sections with a Leica EM TIC 3X Broad Ion Beam (BIB) milling system. The microstructure of the oxide layers was investigated by a JEOL JSM-7800F Prime SEM with an Oxford Instruments Energy-Dispersive X-ray spectrometer using 10 kV for imaging and 15 kV for EDXS.

EDXS of the electrodes was performed with a Quanta FEG 650 scanning electron microscope equipped with a Bruker Quantax 400 SSD energy-dispersive X-ray detector. Processing of data was performed using the Bruker ESPRIT software package.

Results and Discussion

In the following section, the impact of the protective coating for the stack-like contacting is shown by measured IV-characteristics and compared to the defined ideal case.

IV-characteristics.—Figure 2 shows that the ideal contacting with ceramic flow fields reaches the highest performance in electrolysis mode at $T = 850$ °C with 0.2 atm H_2 (balance H_2O) and air at the air electrode. The lowest benchmark was defined for stack-like contacting with uncoated Crofer 22 APU flow fields without LSCF contact paste at the air side (denoted Crofer 22 APU*). Subsequently, it indicates the lowest performance as seen in Fig. 2. All other configurations of contacting perform between the higher and lower benchmark as expected. The uncoated steel grades show a substantial deviation from ideal behavior. Uncoated AISI 441 indicates a somewhat higher performance as compared with uncoated Crofer 22 APU and UNS S44330. The application of the CeCo protective coating on the MICs generates a significant performance increase. All coated MICs reach a maximum current density that is similar to the ideal behavior and thus cannot be clearly separated from each other. The performance variations are in the range of nominally identical ideally contacted cells (+/− 0.02 A cm^{-2} at 1.4 V) and thus should not be related to the applied steel grade.

In order to analyze the impact of the MIC-contacting on the fuel side, an ideal contacting of the air side was combined with the stack like contacting at the fuel side (Fig. 3). When measuring the voltage between gold mesh (AE) and MIC (FE), a similar performance results when measured between gold mesh (AE) and nickel grid

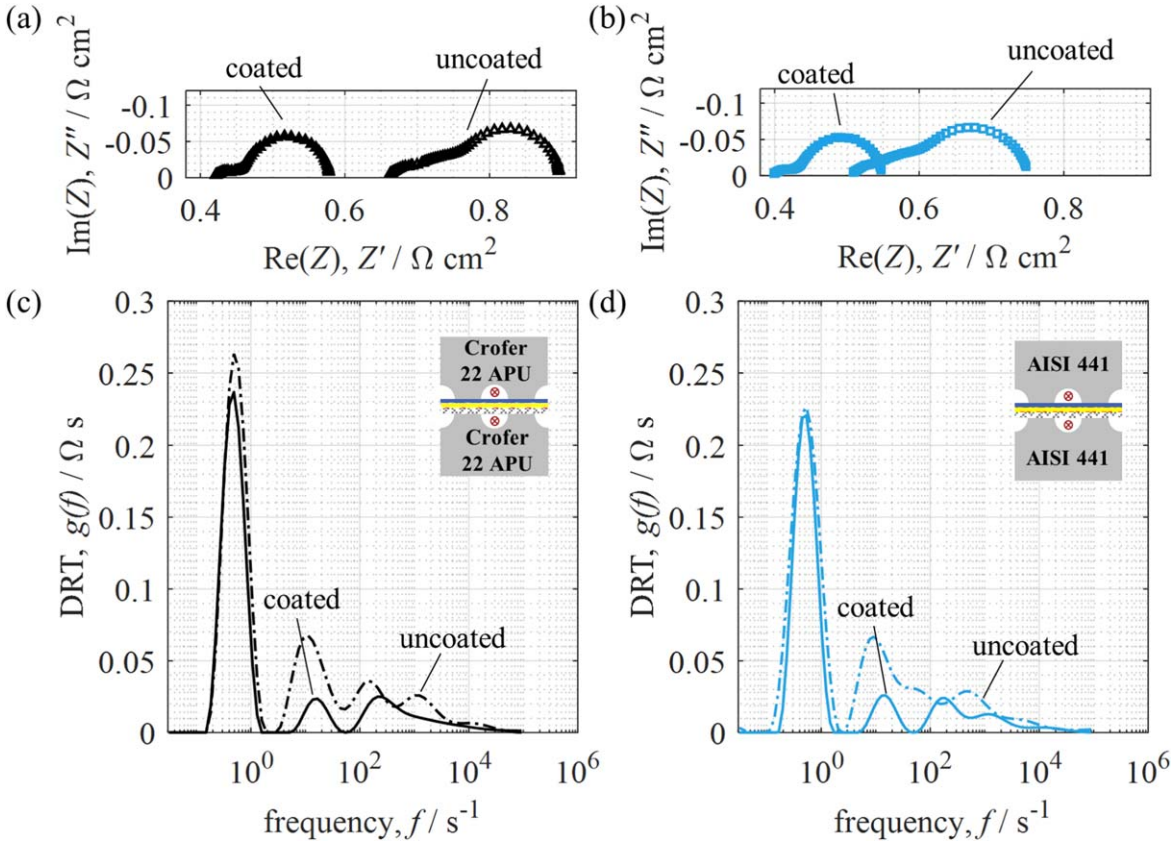

Figure 6. (a) Impedance spectra and (c) DRT of Crofer 22 APU (un-/coated) and (b) and (d) of AISI 441 (un-/coated) at $T = 850$ °C with 0.95 atm H_2 (balance H_2O) and air at the air electrode.

(FE). The stack-like contacting at the air side is mainly responsible for the performance decrease, which might be related to Cr-poisoning and an enhanced contact resistance related to oxide scales on the MIC.

Contact loss air side.—Further investigations with targeted measurements of potential probes at fuel and air side were conducted in order to determine the individual contact losses. In case of an ideal contacting the resistance between gold mesh/LSM-electrode and Ni mesh/Ni-YSZ electrode at 850 °C is < 3 mΩ cm^2 and < 2 mΩ cm^2 respectively.[55] With respect to the fuel side, contact losses can be neglected (< 5 mΩ cm^2). Thus, the point welded finely meshed Ni-grid provides sufficient contacting of the fuel electrode's surface.

Figure 4 presents voltage losses in electrolysis mode due to contacting at the air side at $T = 850$ °C with 0.20 atm H_2 (balance H_2O) and air at the air electrode and compares un-/coated Crofer 22 APU as well as AISI 441. Coating of the MICs with CeCo shows a significant decrease of the measured contact loss with a comparably larger decrease for Crofer 22 APU. The corresponding contact resistances extracted from the slope ($R_{\text{contact,AE}} = \frac{\partial \eta_{\text{contact,AE}}}{\partial j}$) are summarized in Table I. Additionally, the difference of the contact resistance $\Delta R_{\text{contact,AE}}$ between un-/coated MICs is given as well. Similar results were observed in fuel cell mode as well and are not shown here.

IV-characteristics of ideal contacting are again shown in Fig. 5 in comparison to the resulting voltage of the potential difference between $\varphi_{\text{MIC,FE}}$ and $\varphi_{\text{MIC,AE}}$ as well as $\varphi_{\text{mesh,FE}}$ and $\varphi_{\text{probe,AE}}$ of uncoated Crofer 22 APU. When regarding the difference between the mesh at the fuel side $\varphi_{\text{mesh,FE}}$ and the probe at the air side onto the air electrode $\varphi_{\text{probe,AE}}$ the contact losses of the MICs are excluded. Thus, a performance like the ideal case becomes visible. The decrease of performance is thus mainly dominated by the contact loss $\eta_{\text{contact,AE}}$ at the air side of uncoated Crofer 22 APU.

To further evaluate the loss contributions, coated MICs are compared with uncoated substrates by electrochemical impedance spectroscopy and the subsequent analysis of the distribution of relaxation times.

Impedance analysis.—Figure 6 shows the impedance spectra in (a) for Crofer 22 APU and (b) for AISI 441 at $T = 850$ °C with 0.95 atm H_2 (balance H_2O) and air at the air electrode. The ohmic resistance is significantly decreased by the applied CeCo coating for both substrates (Crofer 22 APU 36%, AISI 441 22%).

Ohmic resistance: impedance vs potential probes.—The difference of the ohmic resistance $\Delta R_{0,\text{EIS}}$ extracted from the impedance measurements between un-/coated MICs is given in Table I and should be related to the difference of contact resistance between un- and coated MICs. For Crofer 22 APU, the determination of the difference of the contact resistance at the air side $\Delta R_{\text{contact,AE}}$ by potential probes results in a deviation of 67 mΩ cm^2 in comparison to $\Delta R_{0,\text{EIS}}$. However, for AISI 441 both methods deliver similar values.

Polarization resistance.—The corresponding distribution of relaxation times (DRT) are shown in Figs. 6c, 6d. With respect to cells exhibiting a Ni/GDC fuel electrode an overlap of processes in the spectra needs to be considered.[68–75] Several processes are overlapping underneath the lowest frequency peak such as gas diffusion and activation polarization at the fuel side. Gas diffusion losses at the air side might be coming into effect as well.[66,76] In the mid frequency range from 10 Hz to approx. 10^3 Hz the stack-like contacting with CeCo coating shows a decrease in the polarization

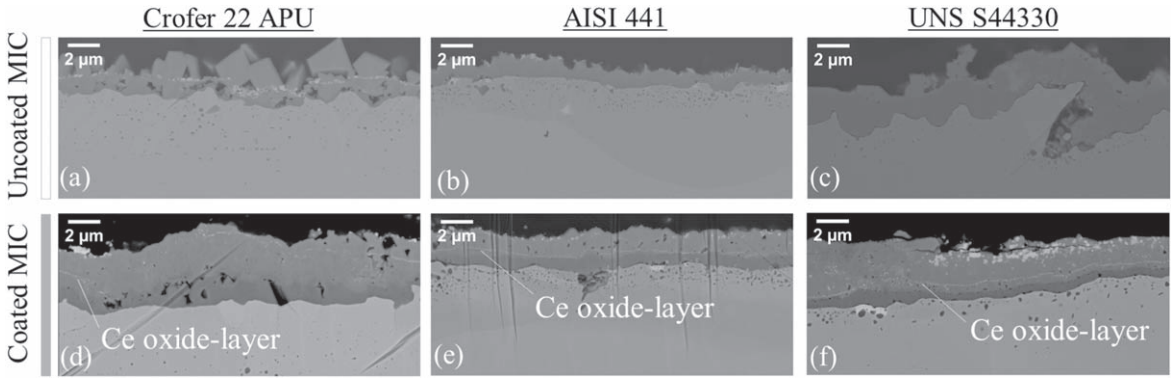

Figure 7. SEM backscattered electron micrographs of the air side of un-/coated (a, d) Crofer 22 APU, (b, e) AISI 441, (c, f) UNS S44330 tested for approx. 200 h.

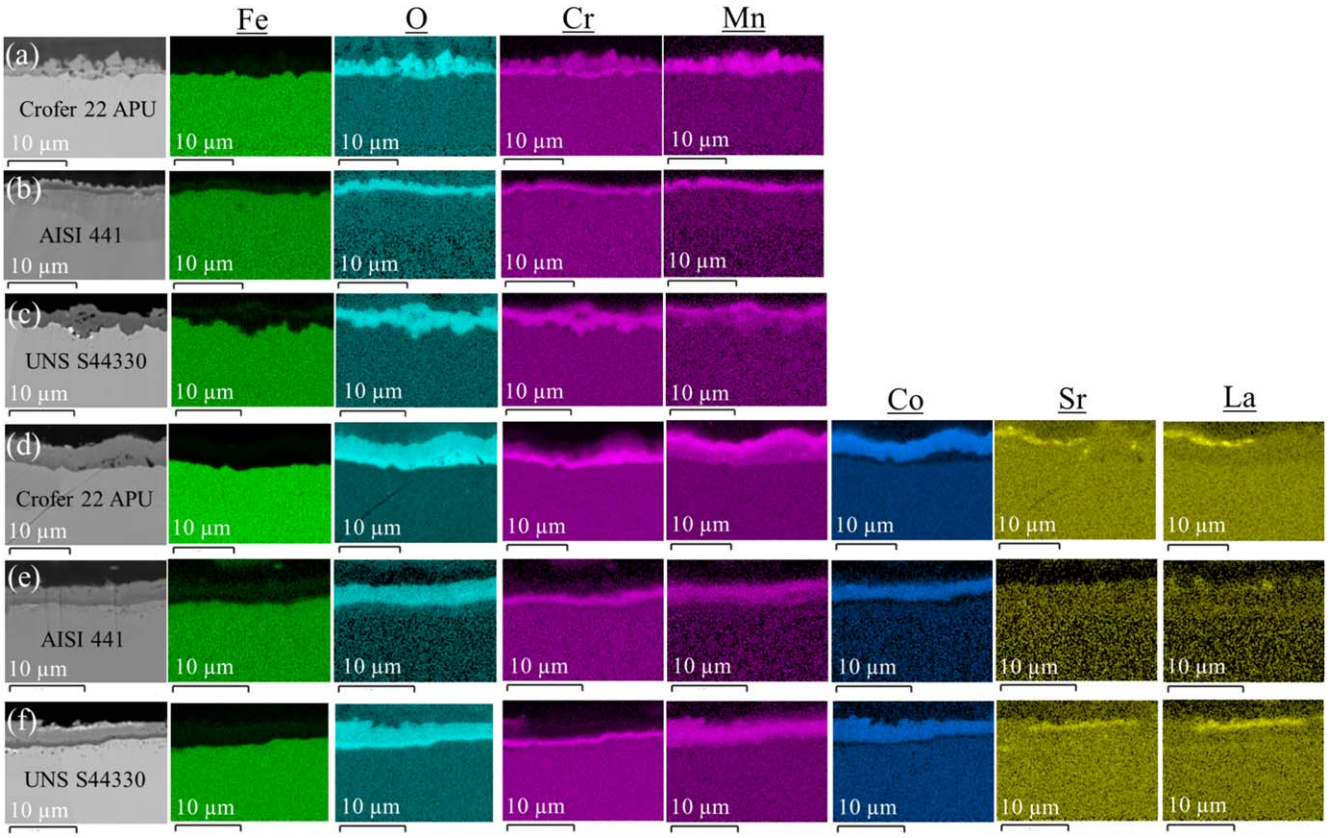

Figure 8. EDXS-Analysis of the air side oxide scale of un-/coated (a, d) Crofer 22 APU, (b, e) AISI 441, (c, f) UNS S44330.

Table I. Extracted contact resistance $R_{contact,AE}$ related to Fig. 4 for un-/coated Crofer 22 APU and AISI 441 with calculated difference between un-/coated substrates $\Delta R_{contact,AE}$ at 850 °C. Difference of the ohmic resistance $\Delta R_{0,EIS}$ related to Fig. 6 by impedance spectroscopy at 850 °C.

Material	Uncoated $R_{contact,AE}$ [Ω cm^2]	Coated $R_{contact,AE}$ [Ω cm^2]	$\Delta R_{contact,AE}$ [Ω cm^2]	$\Delta R_{0,EIS}$ [Ω cm^2]
Crofer 22 APU	0.325	0.021	0.304	0.237
AISI 441	0.132	0.013	0.119	0.112

resistance by approx. 30%. Typically, the surface exchange process at the air electrode can be found in this frequency range.[58,60] An impact of Cr-poisoning to this process needs to be considered and may influence the shape of peaks in the DRT. The lower polarization resistance might be referred to less Cr-evaporation of the MIC at the air side due to the protective coating and thus a lower negative impact. However, in terms of process assignment of the peaks, those cannot be fully dedicated to the air electrode as processes of the fuel side overlap as well.[60] The overall polarization R_{pol} resistance is summarized in Table II.

In the following, the electrochemical results will be correlated to the oxide scales formed on the different MICs and chromium in the air electrode.

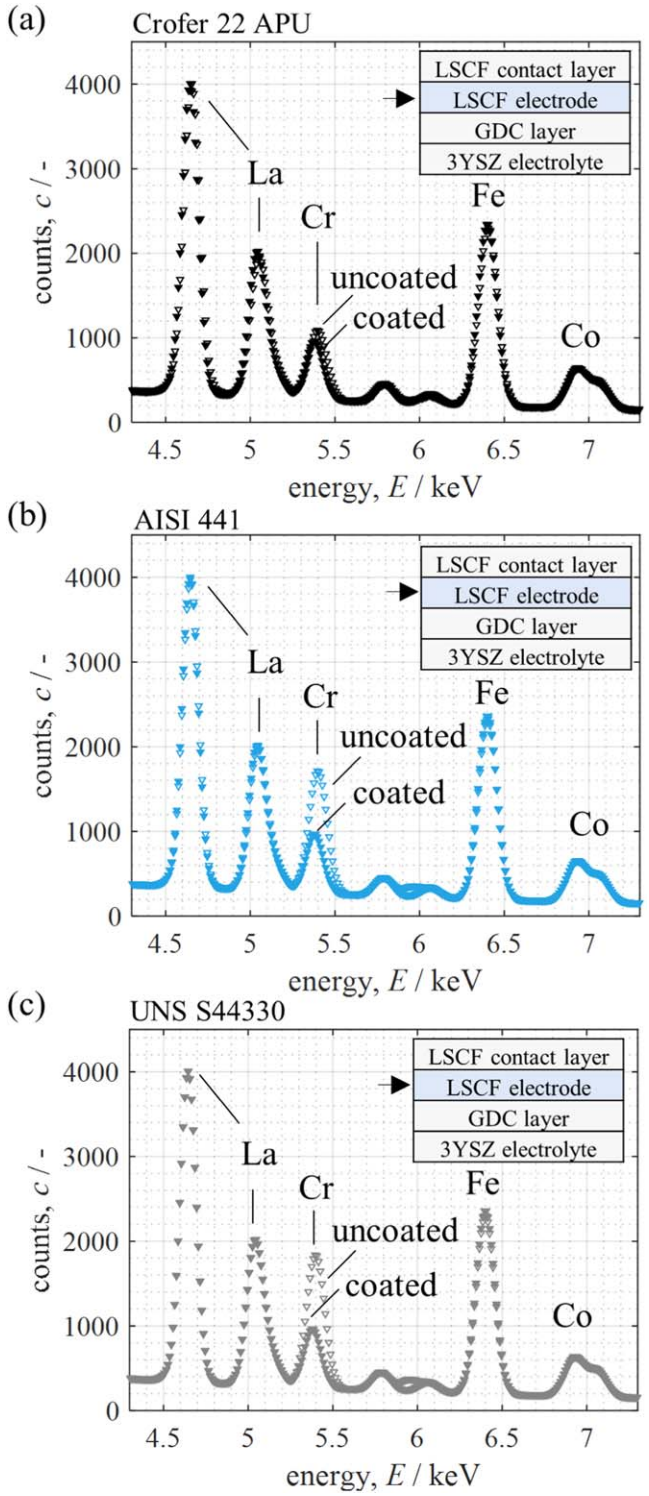

Figure 9. Extraction of energy-dispersive X-ray spectra of the LSCF air electrode contacted with un-/coated (a) Crofer 22 APU, (b) AISI 441 and (c) UNS S44330.

Microstructure analysis.— *Metallic interconnectors.*—With the help of the microstructural analysis of the metallic interconnectors, further insights on the basis of the electrochemical characterization can be obtained. Figure 7 shows SEM cross sections of MICs of the three different steel grades with un-/coated in (a, d) Crofer 22 APU, (b, e) AISI 441, (c, f) UNS S44330. Uncoated samples show significant variation in thickness and microstructure of the oxide scales. In comparison, the coated samples show quite similar thickness and microstructures of the oxide scales. Here, the comparably very thin Ce oxide-layer (10 – 20 nm) of the PVD-coating[24] appears as indicated in the figure. This behavior is similar to earlier findings by Reddy et al.[18]

The EDXS-results are presented in Fig. 8 with (a-c) un- and (d-f) CeCo coated Crofer 22 APU, AISI 441 and UNS S44330. Starting from the iron (Fe)-rich bulk of the MIC appearing in green, different oxide (O) layers become visible at the surface. In case of all uncoated MICs in Figs. 8a–8c, a chromium-rich oxide layer is found that is significantly thicker for uncoated UNS S44330 in comparison to uncoated Crofer 22 APU and AISI 441. Further, a manganese (Mn) rich layer is visible at the surface due to formation of a Cr-Mn-spinel at the surface of the different MICs as observed by Reddy et al.[18]

As shown in Fig. 8 uncoated AISI 441 exhibits the thinnest Cr-oxide layer which can be correlated to the lower contact resistance (Table I) in comparison to Crofer 22 APU.

With respect to the CeCo coated metallic interconnectors, similar thickness of Cr_2O_3 oxide scale can be observed in Figs. 8d–8f. This supports the electrochemical measurement since coated MICs show a performance and contact loss close to the ideal, chromium free contact set-up with ceramic flow fields. Moreover, the thinner chromia scale and lower Cr outward diffusion into the cathode in the presence of CeCo coating resulted in improved contact resistance compared to the uncoated substrates. In contrast to the uncoated samples, a cobalt (Co) layer is visible for all CeCo coated samples indicating the formation of a Co-Mn spinel layer at the surface, as also observed by Reddy et al.[18] This Co-Mn layer has a higher conductivity[77] in comparison to a Cr-Mn spinel for the uncoated samples. The thin (10 – 20 nm) cerium oxide layer is not visible in the EDXS. Further, strontium (Sr) and lanthanum (La) can be observed above the Co-Mn rich oxide layer for Crofer 22 APU and UNS S44330, which is presumably related to the application of the LSCF contact layer and the sintering process during the start- and heat-up phase prior to cell testing.

Cr-poisoning air electrode.—As a result of the higher polarization resistance, the air electrode is analyzed post-mortem by SEM-EDXS with respect to Cr-poisoning of the air electrode. A SEM graph of a comparable electrode is shown in the work by Kullmann et al.[63] With respect to the EDXS measurements, different locations of the LSCF layer were investigated with overall areas between approx. 3000 – 5000 μm^2 for each cell. Thus, an extraction of the energy-dispersive X-ray spectra is shown as a mean value between the different locations in Fig. 9 for un-/coated (a) Crofer 22 APU, (b) AISI 441 and (c) UNS S44330. For comparability, all spectra are normalized to the peak of lanthanum (La), as it is assumed that all samples have the same amount of La in the dedicated LSCF layer. Un-/coated Crofer 22 APU (Fig. 9a) has the smallest difference in the spectra in comparison to the other two substrates. For the peak of Cr, a clear difference can be observed in Figs. 9b and 9c between un-/coated AISI 441 and UNS S44330. However, a detailed microstructural analysis of secondary phase formation and its distribution still needs to be carried out.

Table II shows the quantitative analysis of the EDXS measurements with the mean value of the Cr content $\bar{x}_{Cr}$ in the LSCF layer. It has to noted, that the measurement technique undergoes within certain limits as shown by the standard deviations σ_{Cr} in Table I. Nevertheless, in case of coated substrates similar polarization resistances with almost no chromium in the LSCF layer are found. The CeCo coating blocks the Cr-evaporation effectively. Also, neglectable amounts of chromium were found in the fuel electrode and are not shown here.

Conclusions

In this work, different steel grades (Crofer 22 APU, AISI 441, UNS S44330) were investigated with respect to their impact on the electrochemical behavior of single cells and microstructure of the metallic interconnectors in the un- as well as CeCo coated state for stack-like

Table II. Overall polarization resistance R_{pol} of the cell at 850 °C with 0.95 atm H_2 (balance H_2O) in contact with un-/coated Crofer 22 APU, AISI 441 and UNS S44330. Mean values of the Cr content $\bar{x}_{Cr}$ as well as standard deviation σ_{Cr} in the LSCF layer by EDXS analysis.

	Crofer 22 APU			AISI 441			UNS S44330		
	R_{pol} [Ω cm^2]	$\bar{x}_{Cr}$ [at%]	σ_{Cr} [at%]	R_{pol} [Ω cm^2]	$\bar{x}_{Cr}$ [at%]	σ_{Cr} [at%]	R_{pol} [Ω cm^2]	$\bar{x}_{Cr}$ [at%]	σ_{Cr} [at%]
uncoated	0.242	3.12	(+/−) 2.91	0.242	9.35	(+/−) 4.57	0.425	11.08	(+/−) 0.98
coated	0.160	0.62	(+/−) 0.48	0.153	0.66	(+/−) 0.32	0.163	0.56	(+/−) 0.48

contacting of an electrolyte-supported cell with a Ni/GDC fuel electrode and LSCF air electrode. In the uncoated state electrochemical measurements revealed substantial performance and contact losses. The differences in between the substrates might be correlated to different Cr-oxide scale layers of the MICs at the air side. The lack of an effective cap layer to impede Cr poisoning of the LSCF electrode inhibits a performance closely to the ideal contact set-up with ceramic flow fields. In comparison, the protective CeCo coating of metallic interconnectors showed a characteristic initial performance closely to the ideal contact set-up. For coated substrates, the performance seemed independent of the substrate material itself as similar Cr-oxide scales as well as Co-Mn-Oxide layers are formed at the air side. Coating of the MIC decreases the contact resistance at the air side significantly. Further, the polarization resistance is decreased which is related to less Cr-evaporation at the air electrode as shown by SEM-EDXS-analysis. Thus, electrochemical measurements are successfully coupled with microstructure analysis of the metallic interconnectors as well as of the air electrode. In summary, a protective coating on the metallic interconnector at the air side is essential to achieve a high performance of a solid oxide cell stack.

Acknowledgments

The authors gratefully acknowledge funding from the Helmholtz project “Solar Hydrogen: high purity and compressed” (38.03.02) and from the Federal Ministry of Education and Research (BMBF 03HY124C). Sincere thanks are given to Kerafol GmbH for providing the electrolyte substrates as well as to Sunfire GmbH for producing the test cells. Alleima AB made the coating for the metallic interconnectors gratefully available. The LSCF contact paste was thankfully provided by Norbert Menzler from Forschungszentrum Jülich GmbH, Institute of Energy and Climate Research (IEK), IEK-1: Materials Synthesis and Processing. Further acknowledgment is given to the open access funding provided by the KIT Publication Fund of the Karlsruhe Institute of Technology, Germany.

Appendix

The chemical composition of the three steel grade substrates is listed in the appendix in Tables A·1 and A·2.

Table A·1. Chemical composition of the uncoated steel grade substrates.

Material —	C %	Si %	Mn %	P %	S %	Cr %	Ni %	Ti %
Crofer 22 APU	0.004	0.02	0.44	0.003	<0.002	22.6	0.02	0.06
AISI 441 (1.4509)	0.017	0.41	0.39	0.025	0.001	17.6	0.14	0.13
UNS S44330 (1.4622)	0.015	0.47	0.39	0.029	<0.001	21	0.2	0.14

Table A·2. Part II Chemical composition of the uncoated steel grade substrates.

Material —	Nb %	N %	Cu %	Mo %	Al %	Mg	La	Fe %
Crofer 22 APU	<0.01	0.002	0.01	<0.01	0.013	<0.01	0.1	Bal.
AISI 441 (1.4509)	0.384	—	—	—	—	—	—	Bal.
UNS S44330 (1.4622)	0.36	0.015	0.33	—	—	—	—	Bal.

ORCID

C. Grosselindemann https://orcid.org/0000-0002-9965-843X
D. Esau https://orcid.org/0000-0001-8386-1030
M. Dorn https://orcid.org/0009-0005-1885-7031
F. M. Bauer https://orcid.org/0009-0003-3995-7651
D. Ewald https://orcid.org/0000-0001-8673-0140
J. Froitzheim https://orcid.org/0000-0001-6339-6004
A. Weber https://orcid.org/0000-0003-1744-3732

References

1. J. C.-W. Mah, A. Muchtar, M. R. Somalu, and M. J. Ghazali, *Int. J. Hydrog. Energy*, **42**, 9219 (2017).
2. J. W. Fergus, *Mater. Sci. Eng. A*, **397**, 271 (2005).
3. D. Udomsilp, C. Lenser, O. Guillon, and N. H. Menzler, *Energy Technol.*, **9**, 2001062 (2021).
4. M. Ivanova et al., *Angew. Chem. Int. Ed.*, **62**, 1–25 e202218850 (2023).
5. D. Esau, C. Grosselindemann, S. P. Sckuhr, F. Kullmann, L. Wissmeier, and A. Weber, *ECS Trans.*, **111**, 871 (2023).
6. A. Kromp, A. Leonide, A. Weber, and E. Ivers-Tiffée, *J. Electrochem. Soc.*, **158**, B980 (2011).
7. I. Antepara, I. Villarreal, L. M. Rodriguez-Martinez, N. Lecanda, U. Castro, and A. Laresgoiti, *J. Power Sources*, **151**, 103 (2005).
8. W. J. Quadakkers, J. Piron-Abellan, V. Shemet, and L. Singheiser, *Mater. at High Temp.*, **20**, 115 (2003).
9. P. Kofstad and R. Bredesen, *Solid State Ion*, **52**, 69 (1992).
10. N. Shaigan, W. Qu, D. G. Ivey, and W. Chen, *J. Power Sources*, **195**, 1529 (2010).
11. M. J. Reddy, A. Visibile, J.-E. Svensson, and J. Froitzheim, *Int. J. Hydrog. Energy*, **48**, 14406 (2023).
12. S. Megel et al., *ECS Trans.*, **57**, 89 (2013).
13. M. Preininger, J. Wurm, V. Subotić, R. Schauperl, and C. Hochenauer, *Int. J. Hydrog. Energy*, **42**, 28653 (2017).
14. M. J. Reddy et al., *J. Power Sources*, **568**, 232831 (2023).
15. B. Talic, S. Molin, P. V. Hendriksen, and H. L. Lein, *Corros. Sci.*, **138**, 189 (2018).
16. C. Geipel et al., *ECS Trans.*, **91**, 123 (2019).
17. B. Talic, K. Norrman, T. Sand, J. Froitzheim, and P. V. Hendriksen, *J. Electrochem. Soc.*, **170**, 124517 (2023).
18. M. J. Reddy, T. E. Chausson, J. E. Svensson, and J. Froitzheim, *Int. J. Hydrog. Energy*, **48**, 12893 (2023).
19. A. Topcu, B. Öztürk, and Ö. N. Cora, *Int. J. Hydrog. Energy*, **47**, 3437 (2022).
20. M. Kornely, A. Neumann, N. H. Menzler, A. Leonide, A. Weber, and E. Ivers-Tiffée, *J. Power Sources*, **196**, 7203 (2011).
21. R. Sachitanand, M. Sattari, J.-E. Svensson, and J. Froitzheim, *Int. J. Hydrog. Energy*, **38**, 15328 (2013).
22. F. Mohsenifar, A. Irannejad, and H. Ebrahimifar, *J. Electrochem. Soc.*, **170**, 124502 (2023).
23. B. Talic, V. Venkatachalam, P. V. Hendriksen, and R. Kiebach, *J. Alloys Compd.*, **821**, 153229 (2020).
24. C. Bernuy-Lopez, U. Bexell, M. Stenstrom, N. Norrby, and J. Westlinder, *ECS Trans.*, **103**, 1803 (2021).
25. J. H. Zhu, D. A. Chesson, and Y. T. Yu, *J. Electrochem. Soc.*, **168**, 114519 (2021).
26. P. Gannon, M. Deibert, P.- White, R. Smith, H. Chen, W. Priyantha, J. Lucas, and V. Gorokhovsky, *Int. J. Hydrog. Energy*, **33**, 3991 (2008).
27. N. S. Waluyo, S.-S. Park, R.-H. Song, S.-B. Lee, T.-H. Lim, J.-E. Hong, K. H. Ryu, W. B. Im, and J.-W. Lee, *Ceram. Int.*, **44**, 11576 (2018).
28. M. Tomas, A. Visibile, J.-E. Svensson, and J. Froitzheim, *Int. J. Hydrog. Energy*, **48**, 18405 (2023).
29. J.-E. Hong, M. Bianco, J. V. Herle, and R. Steinberger-Wilckens, *ECS Trans.*, **68**, 1581 (2015).
30. N. Grünwald, D. Sebold, Y. J. Sohn, N. H. Menzler, and R. Vaßen, *J. Power Sources*, **363**, 185 (2017).
31. J. Puranen et al., *Int. J. Hydrog. Energy*, **39**, 17284 (2014).
32. T. Brylewski, J. Dabek, K. Przybylski, J. Morgiel, and M. Rekas, *J. Power Sources*, **208**, 86 (2012).
33. M.-J. Tsai, C.-L. Chu, and S. Lee, *J. Alloys Compd.*, **489**, 576 (2010).
34. S.-I. Lee, J. Hong, H. Kim, J.-W. Son, J.-H. Lee, B.-K. Kim, H.-W.- Lee, and K. J. Yoon, *J. Electrochem. Soc.*, **161**, F1389 (2014).
35. Y. Liu and D. Y. Chen, *Int. J. Hydrog. Energy*, **34**, 9220 (2009).
36. A. G. Sabato, E. Zanchi, S. Molin, G. Cempura, H. Javed, K. Herbrig, C. Walter, A. R. Boccaccini, and F. Smeacetto, *J. Eur. Ceram. Soc.*, **41**, 4496 (2021).
37. J. H. Zhu, Y. Zhang, A. Basu, Z. G. Lu, M. Paranthaman, D. F. Lee, and E. A. Payzant, *Surf. Coat. Technol.*, **177**, 65 (2004).
38. N. Manjunath, K. Santhy, and B. Rajasekaran, *Int. J. Hydrog. Energy*, **48**, 31767 (2023).
39. P. Piccardo, R. Spotorno, and C. Geipel, *Energies*, **15**, 3548 (2022).
40. G. Ghiara, P. Piccardo, V. Bongiorno, L. Repetto, C. Geipel, and R. Spotorno, *Int. J. Hydrog. Energy*, **46**, 23815 (2021).
41. G. Ghiara, P. Piccardo, V. Bongiorno, C. Geipel, and R. Spotorno, *Energies*, **13**, 6487 (2020).
42. M. Kusnezoff, N. Trofimenko, M. Müller, and A. Michaelis, *Materials*, **9**, 906 (2016).
43. 'Sanergy™ HT.' Accessed: May 06, 2024. [Online]. Available: https://www.alleima.com/en/products/coated-strip-steel/sanergy-ht/ (2024).
44. C. Goebel, R. Berger, C. Bernuy-Lopez, J. Westlinder, J.-E. Svensson, and J. Froitzheim, *J. Power Sources*, **449**, 227480 (2020).
45. C. Goebel, V. Asokan, S. Khieu, J.-E. Svensson, and J. Froitzheim, *Surf. Coat. Technol.*, **428**, 127894 (2021).
46. N. Norrby, S. Li, M. Stenström, and J. Westlinder, *ECS Trans.*, **111**, 2223 (2023).
47. J. Froitzheim, H. Ravash, E. Larsson, L. G. Johansson, and J. E. Svensson, *J. Electrochem. Soc.*, **157**, B1295 (2010).
48. S. Dierickx, T. Mundloch, A. Weber, and E. Ivers-Tiffée, *J. Power Sources*, **415**, 69 (2019).
49. A. Weber, *tm - Technisches Messen*, **88**, 1–16 (2021).
50. M. Kornely, N. H. Menzler, A. Weber, and E. Ivers-Tiffée, *Fuel Cells*, **13**, 506 (2013).
51. J. Froitzheim, S. Canovic, M. Nikumaa, R. Sachitanand, L. G. Johansson, and J. E. Svensson, *J. Power Sources*, **220**, 217 (2012).
52. A. Beez, X. Yin, N. H. Menzler, R. Spatschek, and M. Bram, *J. Electrochem. Soc.*, **164**, F3028 (2017).
53. N. H. Menzler, D. Sebold, and Q. Fang, *J. Electrochem. Soc.*, **162**, F1275 (2015).
54. S. Fontana, R. Amendola, S. Chevalier, P. Piccardo, G. Caboche, M. Viviani, R. Molins, and M. Sennour, *J. Power Sources*, **171**, 652 (2007).
55. A. Weber, *tm - Technisches Messen*, **89**, 97 (2022).
56. A. Leonide, V. Sonn, A. Weber, and E. Ivers-Tiffée, *J. Electrochem. Soc.*, **155**, B36 (2007).
57. J.-C. Njodzefon, D. Klotz, A. Kromp, A. Weber, and E. Ivers-Tiffée, *J. Electrochem. Soc.*, **160**, F313 (2013).
58. A. Leonide, Y. Apel, and E. Ivers-Tiffee, *ECS Trans.*, **19**, 81 (2009).
59. V. Sonn, A. Leonide, and E. Ivers-Tiffée, *J. Electrochem. Soc.*, **155**, B675 (2008).
60. C. Grosselindemann, N. Russner, S. Dierickx, F. Wankmüller, and A. Weber, *J. Electrochem. Soc.*, **168**, 124506 (2021).
61. M. Kornely, A. Leonide, A. Weber, and E. Ivers-Tiffée, *J. Power Sources*, **196**, 7209 (2011).
62. M. W. Lundberg, R. Berger, J. Westlinder, and H. Holmberg, *ECS Trans.*, **68**, 1681 (2015).
63. F. Kullmann, C. Grosselindemann, L. Salamon, F.-M. Fuchs, and A. Weber, *Fuel Cells*, **23**, 420 (2023).
64. D. Klotz, A. Weber, and E. Ivers-Tiffée, *Electrochim. Acta*, **227**, 110 (2017).
65. M. J. Reddy, J.-E. Svensson, and J. Froitzheim, *ECS Trans.*, **103**, 1899 (2021).
66. H. Geisler, A. Kromp, A. Weber, and E. Ivers-Tiffée, *J. Electrochem. Soc.*, **161**, F778 (2014).
67. M. Schönleber, D. Klotz, and E. Ivers-Tiffée, *Electrochim. Acta*, **131**, 20 (2014).
68. V. A. Rojek-Wöckner, A. K. Opitz, M. Brandner, J. Mathé, and M. Bram, *J. Power Sources*, **328**, 65 (2016).
69. M. Riegraf, R. Costa, G. Schiller, K. A. Friedrich, S. Dierickx, and A. Weber, *J. Electrochem. Soc.*, **166**, F865 (2019).
70. A. Nenning, C. Bischof, J. Fleig, M. Bram, and A. K. Opitz, *Energies*, **13**, 987 (2020).
71. A. Weber, S. Dierickx, N. Russner, and E. Ivers-Tiffée, *ECS Trans.*, **77**, 141 (2017).
72. M. Riegraf, V. Yurkiv, R. Costa, G. Schiller, and K. A. Friedrich, *ChemSusChem*, **10**, 587 (2017).
73. A. Hagen, A. K. Padinjarethil, and J. Heijne, *Electrochim. Acta*, **461**, 142672 (2023).
74. F. Kullmann, M. Mueller, A. Lindner, S. Dierickx, E. Mueller, and A. Weber, *J. Power Sources*, **587**, 233706 (2023).
75. C. Grosselindemann, F. Kullmann, T. Lehnert, O. Fritz, F.-M.- Fuchs, and A. Weber, *Fuel Cells*, **23**, 442 (2023).
76. H. Geisler, M. Kornely, A. Weber, and E. Ivers-Tiffée, *ECS Trans.*, **57**, 2871 (2013).
77. X. Chen, P. Y. Hou, C. P. Jacobson, S. J. Visco, and L. C. De Jonghe, *Solid State Ion*, **176**, 425 (2005).